Transition to turbulence behind a traveling plate

Reijtenbagh, Jesse; Westerweel, Jerry; Van De Water, Willem

DOI
10.1103/PhysRevFluids.8.104601

Publication date
2023

Document Version
Final published version

Published in
Physical Review Fluids

Transition to turbulence behind a traveling plate

Jesse Reijtenbagh, Jerry Westerweel, and Willem van de Water*
Laboratory for Aero and Hydrodynamics, Delft University of Technology and J. M. Burgers Centre for Fluid Dynamics, 2628 CD Delft, The Netherlands

(Received 7 March 2023; accepted 5 September 2023; published 5 October 2023)

In our experiment a vortical flow behind a traveling plate turns into turbulence. By exactly repeating this experiment 42 times with a robot, we study the statistics of this transition. In each realization the fate of the flow is followed over 1.7 s when the plate travels with a constant velocity. It suddenly turns turbulent at a scaled traveled distance of $x^* \approx 5.5$. We register the vorticity in a plane that divides the plate perpendicularly. We introduce an original Lagrangian measure of variability between the experiment realizations. The finite-time Lyapunov exponent field of a single experiment predicts this variability; thus we confirm ergodicity. Apart from pointwise measures, yielding a distribution over the field of view, we study the statistics of the circulation computed over the upper and lower half of the domain. The almost perfect symmetry both of the mean and of the fluctuations points to their origin as the fluctuating vortex ring trailing behind the plate. During the initial phase long-time correlations exist in the flow, but they cease once the flow turns turbulent. By ordering our repeated experiments we find that extreme circulations are preceded by circulations that are larger than the median.

DOI: 10.1103/PhysRevFluids.8.104601

I. INTRODUCTION

How vortices form behind a traveling plate was analyzed by Prandtl [1], and an excellent historical account can be found in Koumoutsakos and Shiels [2]. The present paper is about experiments on the flow behind a plate submerged in water that in a short time is accelerated from rest to a velocity of $U = 0.4$ m s^{-1}. Our measurement plane cuts the plate halfway perpendicularly. Initially, a vortex loop is formed that is intersected twice by this plane and shows as a pair of trailing vortices. These vortices merge and become turbulent. By repeating this experiment multiple times using a robot that accurately replicates the plate motion, we focus on the fluctuations in this ensemble.

The course of events in the evolving wake has been documented by Koumoutsakos and Shiels [2] and Fernando and Rival [3], with stages in the vortex formation named by Luchini and Tognaccini [4]. It is illustrated by the result of our experiment in Fig. 1, where we show the vorticity, ensemble averaged over the 42 repetitions of the experiment, at dimensionless plate displacements $x^* = 1, 3, 5, 7$, and $x^* = 8.14$, where the plate leaves the field of view. As nondimensional plate traveling time or plate distance, we use

$$t^* = l_b^{-1} \int_0^t U(t')\, dt', \tag{1}$$

which equals the traveled distance x^* in units of the plate width l_b. This time is called the "formation time" by Gharib *et al.* [5] as it is the timescale for the formation of a vortex ring behind a piston. In

*Corresponding author: w.vandewater@tudelft.nl

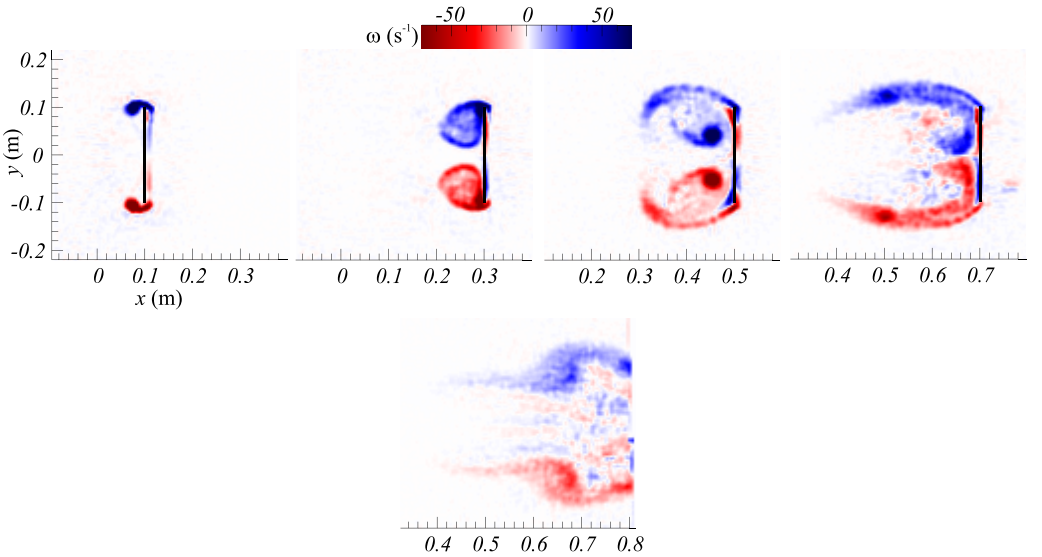

FIG. 1. Ensemble-averaged vorticity at scaled plate distances $x^* = 1, 3, 5, 7, 8.2$. The plate (indicated by the vertical line) leaves the PIV field of view at $x^* = 8.14$. The plate height $l_b = 0.1$ m so that the scaled distance is 10 times the physical traveled distance x in m. The creation of secondary vortices in the shear layers that engulf the separation bubble can be clearly seen. The focus in this paper is on the variations between repeated experiments, which here have been averaged to a small value.

the sequel we interchangeably use the dimensionless t^* and x^*. At around $x^* \gtrsim 3$, the vortices start lagging behind the plate—the vortex expulsion phase [4]. This article deals with the events long after this phase.

Several acceleration scenarios have been studied. Ours, in which the plate is accelerated in the interval $x^* \in [0, 1]$ to a final velocity $U = 0.4\ \mathrm{m\,s^{-1}}$ (see Fig. 2), can be compared to the impulsive start-up case in numerical analyses. As expected, details such as the time dependence of the circulation and the path of the detached vortices depend on the manner in which the plate is accelerated [4,6]. Due to the plate edge singularity, the numerical analysis of the flow is challenging [2,4,7], but simulations agree on the emergence of secondary vortices in the unstable shear layer.

The phenomenology of the evolving flow, briefly summarized above, is not the main point of this paper, but rather the way in which small differences between repeated experiments grow. The origin of this divergence is the sensitive dependence on initial conditions: the butterfly effect. Even though the experiments are repeated with robotic precision, differences between initial conditions are inevitable.

Movies of the evolving velocity field for two arbitrarily selected experiments are provided in the Supplemental Material [8]. Striking to the eye is the initial similarity between experiments, which is gradually eroded as time progresses. This is most noticeable so in the late stage when the starting vortices have detached and secondary vortices have formed in the shear layer that envelops the vortex bubble [2] with the eventually merged vortices evolving into a turbulent wake.

First, we will quantify the divergence of two repeated experiments by measuring the average difference $d_T(\boldsymbol{x}, t)$ between Lagrangian trajectories of fluid parcels that originated at the same location $\boldsymbol{x}$ and the same time t since the start of the plate in different experiments. Initially, the trajectories in different experiments stay close, but their distance grows as time progresses. By construction $d_{T=0}(\boldsymbol{x}, t) = 0$, but $d_T(\boldsymbol{x}, t)$ will grow with increasing delay T because the experiment realizations are slightly different, and the initial position $\boldsymbol{x}$ of a virtual tracer in a 2D slice of the velocity field is an incomplete characterization of the experiment.

The quantity $d_T(\boldsymbol{x}, t)$ is an average over all distinct pairs of experiment realizations. The growth of an infinitesimal distance in a *single* experiment i is gauged by the finite-time Lyapunov exponent (FTLE) field, $\Lambda_{T,i}(\boldsymbol{x}, t)$ which is a property of the velocity field $\boldsymbol{u}_i(\boldsymbol{x}, t)$ [9,10]. The on average exponential growth of small differences is expressed by a positive Lyapunov exponent, whose existence is the essence of chaos. Also turbulence is a chaotic state, characterized by a continual sensitivity to variation of initial conditions, that is, by a positive Lyapunov exponent [11,12]. Even when it would have been possible to initiate repeated experiments with almost molecular precision, chaos will drive them apart, and do that with an exponential rate that is independent of the initial separation.

The FTLE field $\Lambda_T(\boldsymbol{x}, t)$ has become a popular way to visualize flow. Ridges of the FTLE field have been used by Xiang *et al.* [13] to delineate vortex boundaries; they were observed to "faintly" organize the transport of tracers. The FTLE field has also been linked to the way passive tracers are dispersed in an experiment [14–16].

The scalar fields $d_T(\boldsymbol{x}, t)$ and $\Lambda_{T,i}(\boldsymbol{x}, t)$ are both Lagrangian quantities. However, while the FTLE field $\Lambda_{T,i}(\boldsymbol{x}, t)$ gauges the exponential growth of a perturbation in a single experiment realization i, the field $d_T(\boldsymbol{x}, t)$ quantifies the variation over a time T in the entire ensemble, with the initial perturbation set only by the reproducibility of initial conditions. After a while, d_T will be determined by the direction of strongest growth. By measuring d_T after different integration times T, and taking logarithms, a field can be made that can be compared directly to Λ_T. The question then is whether the variability in an entire ensemble can be predicted by computing the FTLE from a single experiment.

The dissimilarity between experiments will be quantified by the error energy $\Delta u^2(t) = \langle |\boldsymbol{u}_i(\boldsymbol{x}, t) - \boldsymbol{u}_j(\boldsymbol{x}, t)|^2 \rangle_{\boldsymbol{x}, i \neq j}$, with averages done over the domain $\boldsymbol{x}$ and experiment realizations $i \neq j = 1, \ldots, 42$. It is a simple instantaneous measure of the correlation between different experiment realizations. As expected, the correlation is large in the stage where the vortices are formed and decreases rapidly in the turbulent stage. In a single realization, but for different locations, the average $\Delta u^2(\delta, t) = \langle |\boldsymbol{u}_i(\boldsymbol{x} + \boldsymbol{\delta}, t) - \boldsymbol{u}_i(\boldsymbol{x}, t)|^2 \rangle_{\boldsymbol{x}, i}$ is the second-order structure function that quantifies the correlation of the velocity field across a separation $\boldsymbol{\delta}$. Analogous quantities can be defined for the vorticity field.

As vorticity plays a central role in this experiment, we will also measure the statistics of circulations Γ_1 and Γ_2 taken over the upper ($y > 0$) and lower ($y < 0$) half of the field of view, respectively. Naturally, the mean values of Γ_1 and Γ_2 have opposite sign. Showing the evolution of $\Gamma_{1,2}$ is one way to characterize vortex formation behind the plate [2]. Through segmentation of the vorticity field, the vortex circulation can be distinguished from the vorticity that remains attached to the plate. Another way to quantify vortex dynamics then is to trace the trajectory of the detached vortices [4,6,7].

The relatively large number of repeats allows an estimate of the average separation $d_T(\boldsymbol{x}, t)$, the mean finite-time Lyapunov field $\Lambda_T(\boldsymbol{x}, t)$, and the correlation between experiments. Previously, experiments, and numerical simulations of the wake shed off a traveling plate have concentrated on phenomenology and vortical phenomena. To the best of our knowledge, this is the first time that ensemble statistics of the transition to turbulence has been studied.

After a description of the experiment in Sec. II, we will discuss the two fields that quantify the divergence of repeated experiments: first, the FTLE field Λ_T in Sec. III A 1, followed by the difference field d_T in Sec. III A 2. The global correlation between experiments can be found in Sec. III B. Finally, results on the fluctuating circulation are presented in Sec. III C.

II. EXPERIMENT

Figure 2 shows the experimental setup. It consists of open-top glass tank with a horizontal cross section of 2 m^2 and a height of 0.6 m, filled with water to a depth of 0.5 m. The flat plate has a width $l_a = 0.2$ m, a height $l_b = 0.1$ m, and a thickness $l_c = 4$ mm. At $x^* = 1$ it reaches its final velocity $U = 0.4$ ms^{-1}. Based on l_b, the Reynolds number is $\mathrm{Re} = 4 \times 10^4$. The plate is attached to an

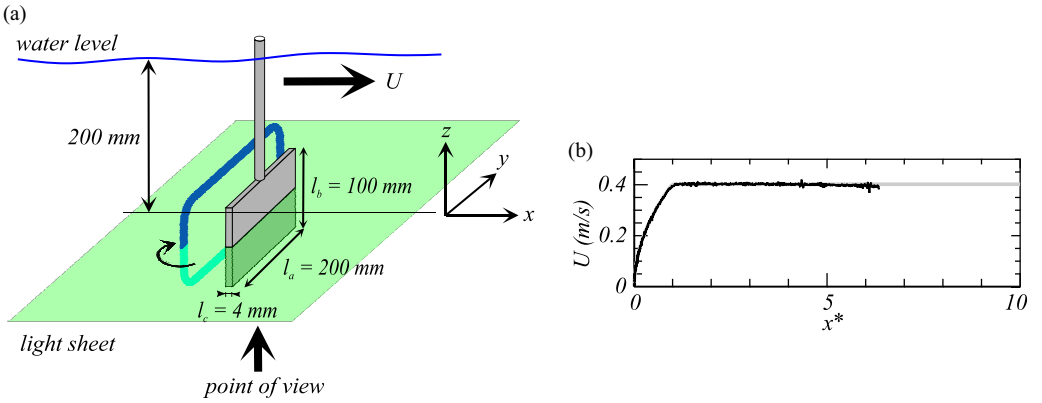

FIG. 2. (a) Schematic view of the plate, coordinate system, and light sheet. The view of the vorticity field is in the positive z direction. The plate is submerged in a tank with dimensions 2×2 m^2 and height of 0.6 m. The trailing vortex loop is indicated schematically; it is intersected by the laser sheet. (b) Black line: measured trace of the velocity of the plate; gray line: as programmed in the robot. The r.m.s. size of the velocity differences is 1%. The plate is accelerated to $U = 0.4$ ms^{-1}, which is reached at dimensionless distance $x^* = 1$.

industrial robot arm (Reis Robotics RL50) with a streamlined strut piercing the air-water interface. The actual velocity of the plate was measured using PIV and a random dot pattern attached to it. After the acceleration phase that ends at $x^* = 1$, the velocity is $U = 0.4$ ms^{-1} with r.m.s. variation $U_{\rm rms} = 0.004$ m s^{-1}. The position of the robot arm reproduces the plate trajectory to within 0.1 mm, during both the acceleration and constant velocity phases. The acquisition of the PIV images was synchronized with the robot motion.

To quantify the flow field we used planar particle image velocimetry (PIV). The field of view is in the horizontal x, y plane through the center of the tranparent plate. A 4 megapixel high-speed camera (Phantom VEO 640 L) was used to capture the flow through the glass bottom upwards in the positive z direction at a frame rate of 1000 f.p.s. Neutrally buoyant fluorescent spherical tracer particles (Cospheric UVPMS-BR-0.995, 53–63 μm diameter) were added to the fluid and were illuminated using a 516 nm Nd-YLF 150 W laser (Litron LDY304-PIV). The acquired images were analyzed using commercial software (LaVision DaVis 10). To create image pairs from the sequential images acquired at 1000 frames per second every nth frame was paired with the $(n + 2)$th frame resulting in a 2 ms exposure time delay. This was chosen to ensure sufficient displacement of the particle images in the region of interest, i.e., the wake behind the plate. A multipass sum-of-correlation PIV algorithm was used to obtain the flow velocity field from the image pairs. The interrogation windows of the three subsequent passes were 48×48 pixels for the first pass, and 24×24 pixels for the second and third passes. A 50% overlap between adjacent interrogation positions was used. This resulted in velocity vector fields with a vector spacing of 4.2 mm. Between two subsequent exposures, the plate moved over 0.8×10^{-3} m. More details of the experimental setup can be found in Grift *et al.* [17].

III. RESULTS

The differences between experimental realizations depend on space and time. Some regions of the flow are less susceptible to small variations in the initial conditions than others. We first discuss pointwise difference fields in Sec. III A. Then, in Sec. III B, we introduce the spatially averaged error field, which reflects the global loss of correlation. Finally the fluctuations of $\Gamma_{1,2}$ between experiment realizations will be discussed in Sec. III C.

A. Pointwise variability

1. Finite-time Lyapunov exponents

Finite-time Lyapunov exponents gauge the exponentially fast spreading of nearby fluid parcels, for either positive or negative times [9,10]. They are computed from the measured velocity field $\boldsymbol{u}_i(\boldsymbol{x},t)$ of a single experiment realization i. In our case the quality of the PIV data warrants the computation of the strain field $\mathbf{A}(\boldsymbol{x},t)=\nabla\boldsymbol{u}(\boldsymbol{x},t)$, so that an infinitesimal separation vector $\boldsymbol{\delta}(t)$ can be integrated along a Lagrangian trajectory,

$$\frac{d\boldsymbol{\delta}}{dt}=\mathbf{A}(\boldsymbol{x}(t),t)\cdot\boldsymbol{\delta}(t),\quad\text{with}\quad\frac{d\boldsymbol{x}(t)}{dt}=\boldsymbol{u}(\boldsymbol{x},t) \tag{2}$$

The time integration of Eq. (2) over an interval t_0, t_0+T, with $\boldsymbol{x}(t_0)=\boldsymbol{x}_0$, defines the evolution matrix $\mathbf{M}_{t_0}^{t_0+T}$ as $\boldsymbol{\delta}(t_0+T)=\mathbf{M}_{t_0}^{t_0+T}\cdot\boldsymbol{\delta}(t_0)$. The largest eigenvalue λ_2 of the positive Cauchy-Green tensor,

$$\mathbf{C}_{t_0}^{t_0+T}=\mathbf{M}_{t_0}^{t_0+T}\left(\mathbf{M}_{t_0}^{t_0+T}\right)^{\dagger}, \tag{3}$$

with † the adjoint, then defines the finite-time Lyapunov exponent $\Lambda_{T,i}(\boldsymbol{x}_0,t)$ of experiment i as

$$\Lambda_{T,i}(\boldsymbol{x}_0,t_0)=\frac{1}{2T}\ln(\lambda_2). \tag{4}$$

For the time interval T we chose $T=0.128$ s, which can be compared to a large eddy turnover time ($l_a/U=0.125$ s), and which corresponds to a plate displacement of 5.1×10^{-2} m. The FTLE field $\Lambda_{T,i}(\boldsymbol{x}_0,t_0)$ was computed for each grid point $\boldsymbol{x}_0=\boldsymbol{x}$ and each plate distance x^*, with x^* and t_0 related as in Eq. (1) (interchangeably we use t^* and x^* to indicate the traveled plate distance).

The FTLE field $\Lambda_{T,i}(\boldsymbol{x},x^*)$ for a single experiment at plate displacements $x^*=1,3,5,7$ is shown in Fig. 3. It is characterized by ridges, some of which occur at random positions in different experiments, and some of which remain in the ensemble average where they delineate the wake structure. At a particular plate displacement $x^*=5$, the ensemble mean and fluctuations of $\Lambda_T(\boldsymbol{x},x^*)$ are shown in Fig. 3(d) and Fig. 3(c), respectively.

If the growth of perturbations were perfectly exponential, $\Lambda_T(\boldsymbol{x},x^*)=\Lambda_{T/2}(\boldsymbol{x},x^*)$. The ratio $\widetilde{\Lambda}_T(\boldsymbol{x},x^*)=\Lambda_T(\boldsymbol{x},x^*)/\Lambda_{T/2}(\boldsymbol{x},x^*)$ is <1 when the growth is slower than exponential and >1 when it is faster than exponential. For the realization at $x^*=5$ in Fig. 1, $\widetilde{\Lambda}_T(\boldsymbol{x},t^*)$ is shown in Fig. 3(b). It demonstrates that the growth of perturbations is indeed mostly exponential.

2. Difference field

The difference field follows from starting a fluid parcel at the same location $\boldsymbol{x}_{i,t}$ and the same time t in all experiment realizations i, tracking all fluid parcels over a time interval T when they have reached $\boldsymbol{x}_{i,t+T}$ in experiment i and $\boldsymbol{x}_{j,t+T}$ in experiment j, and computing the difference

$$d_T(\boldsymbol{x},t)=\frac{\langle|\boldsymbol{x}_{j,t+T}-\boldsymbol{x}_{i,t+T}|\rangle_{i\neq j}}{T}, \tag{5}$$

averaged over all unlike pairs $i\neq j$ of experiment realizations. The difference field $d_T(\boldsymbol{x},x^*)$ at $x^*=1,3,5,7$ is shown in Fig. 4. It is compared to the FTLE field computed over the same time interval $T=0.128$ s. Notice that the magnitude of the fields cannot be compared: $\Lambda_T(\boldsymbol{x},t)$ is the log of a ratio, while $d_T(\boldsymbol{x},t)$ is a length (both per unit of time).

There is a striking similarity between these fields, as expressed by the normalized correlation $C(x^*)$ between them:

$$C(x^*)=\frac{\langle[\Lambda_T(\boldsymbol{x},t)-\langle\Lambda_T(\boldsymbol{x},t)\rangle_{\boldsymbol{x}}][d_T(\boldsymbol{x},t)-\langle d_T(\boldsymbol{x},t)\rangle_{\boldsymbol{x}}]\rangle_{\boldsymbol{x}}}{\left[\left\langle\Lambda_T^2(\boldsymbol{x},t)\right\rangle_{\boldsymbol{x}}-\langle\Lambda_T(\boldsymbol{x},t)\rangle_{\boldsymbol{x}}^2\right]^{1/2}\left[\left\langle d_T^2(\boldsymbol{x},t)\right\rangle_{\boldsymbol{x}}-\langle d_T(\boldsymbol{x},t)\rangle_{\boldsymbol{x}}^2\right]^{1/2}}, \tag{6}$$

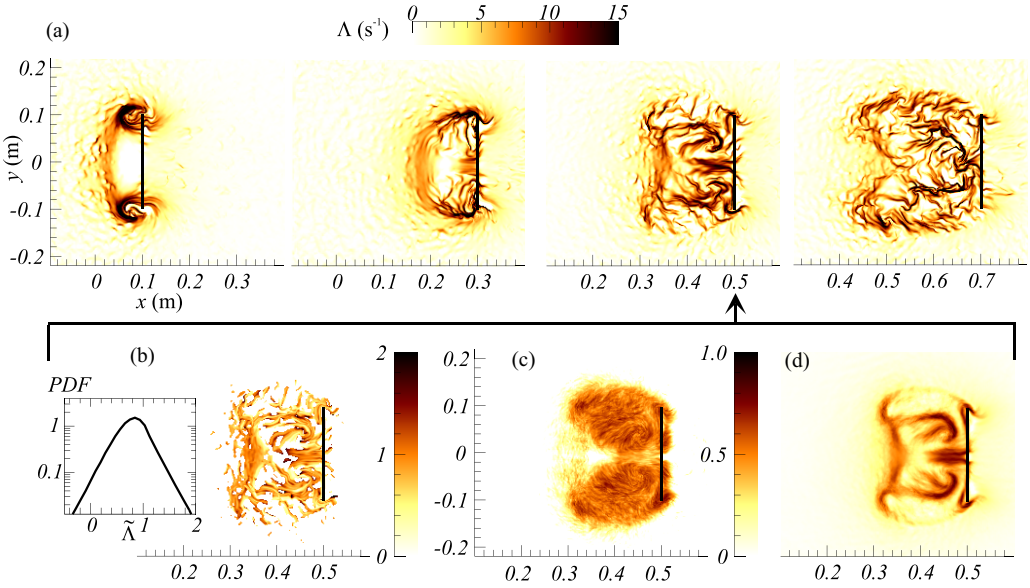

FIG. 3. (a) FTLE field of a single experiment realization at scaled plate distances $x^* = 1, 3, 5, 7$ ($x^* = 10\,x$). The frames at the bottom row all correspond to plate separation $x^* = 5$. (b) Consistency with exponential growth of a single realization [$x^* = 5$ in (a)]. It is quantified by $\widetilde{\Lambda}_T(\boldsymbol{x}, x^*) = \Lambda_T(\boldsymbol{x}, x^*)/\Lambda_{T/2}(\boldsymbol{x}, x^*)$, with $T = 0.128$ s. It is 1 when fluid parcels separate exponentially in time. The inset shows the PDF of $\widetilde{\Lambda}_T$. (c) Root mean square fluctuations $\sigma\Lambda_T$ of FTLE field at $x^* = 5$; the scale is logarithmic. Shown is $\log_{10}\,\sigma\Lambda_T(\boldsymbol{x}, x^*)$, with $\sigma\Lambda_T$ in s^{-1}. (d) Ensemble mean of FTLE field at $x^* = 5$; the scale is the same as that of the top row (a).

where $\Lambda_T(\boldsymbol{x}, t)$ is now the ensemble average $\langle\Lambda_{T,i}(\boldsymbol{x}, t)\rangle_i$, and with x^* and t related as in Eq. (1). This result should be very close to the ensemble-averaged correlation between the individual $\Lambda_{T,i}(\boldsymbol{x}, t)$ and $d_T(\boldsymbol{x}, t)$.

Since $d_T(\boldsymbol{x}, x^*)$ grows from (nominally) $d_T = 0$ at $T = 0$, it cannot be compared directly to the FTLE field, which involves logarithms. As a further refinement we therefore take d_{T_1} at $T_1 = 32$ ms as initial separation and quantify its exponential growth as

$$d_{T_2,T_1}(\boldsymbol{x}, x^*) = \frac{1}{T_2 - T_1} \ln \frac{d_{T_2}(\boldsymbol{x}, x^*)}{d_{T_1}(\boldsymbol{x}, x^*)}, \tag{7}$$

with $T_2 = 128$ ms. The resemblance of d_{T_2,T_1} in Fig. 4(c) with the field $\Lambda_{T_2}(\boldsymbol{x}, x^*)$ is even stronger, but d_{T_2,T_1} is noisy as it involves the velocity fields of different experiments. The equivalence between Λ_{T_2} and d_{T_2,T_1} owes itself to the selection of the direction of strongest growth for an arbitrary perturbation.

3. *Ergodicity*

The strong correlation between the FTLE field $\Lambda_T(\boldsymbol{x}, x^*)$ and the difference fields $d_T(\boldsymbol{x}, x^*)$ and $d_{T_2,T_1}(\boldsymbol{x}, x^*)$, which express the ensemble difference between realizations, is reminiscent of *ergodicity*. It is believed that turbulent flow is ergodic: the statistical properties of an ensemble are the same as those obtained from a time average of a single ensemble member [18,19]. In our case, the temporal dynamics of a single ensemble member predicts the variability in the entire ensemble.

B. Error energy

Both the FTLE field $\Lambda_T(\boldsymbol{x}, x^*)$ and the difference field $d_T(\boldsymbol{x}, x^*)$ are Lagrangian and involve the evolution over a time interval T. The *instantaneous* difference between the velocity fields of our

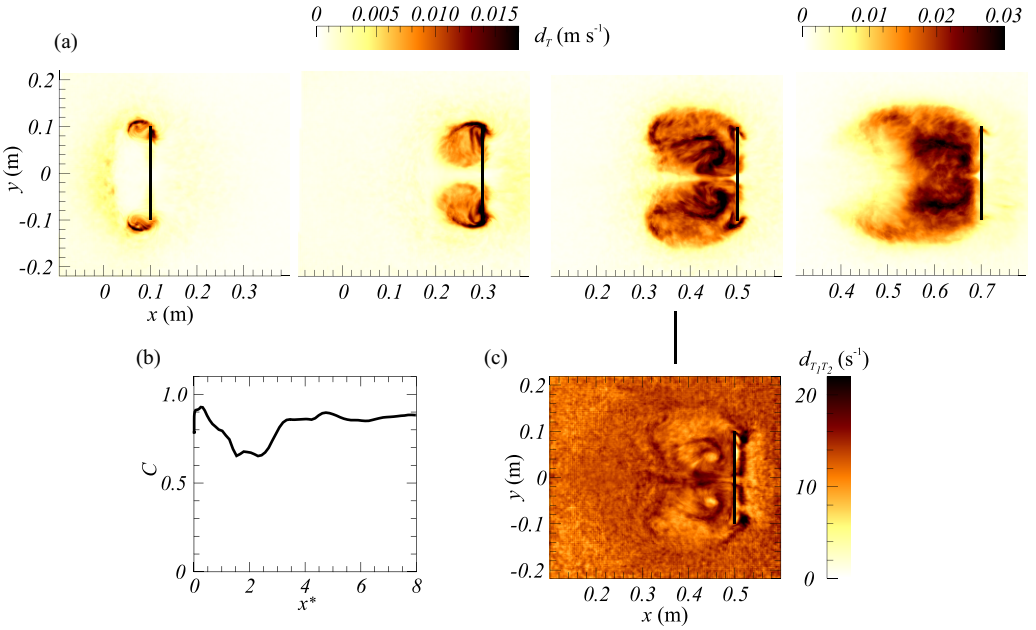

FIG. 4. (a) Difference field $d_T(\boldsymbol{x}, x^*)$ at scaled plate distances $x^* = 1, 3, 5, 7$ ($x^* = 10\,x$). An average was done over all 861 distinct pairs of the ensemble. Notice the change of scale at $x^* = 7$. (b) Normalized correlation with the (ensemble-averaged) FTLE field $\lambda_T(\boldsymbol{x}, x^*)$. At $x* = 5$, $d_T(\boldsymbol{x}, x^*)$ can be compared to $\lambda_T(\boldsymbol{x}, x^*)$ in Fig. 3(d). (c) Logarithmic difference field, d_{T_2,T_1}, [Eq. (5)] with $T_1 = 32$ ms and $T_2 = 128$ ms. It should be compared to the ensemble mean FTLE field in Fig. 3(d).

ensemble can be expressed using the normalized error energy:

$$\Delta\widetilde{u}^2(x^*) = \frac{\langle|\widetilde{\boldsymbol{u}}_i(\boldsymbol{x}, x^*) - \widetilde{\boldsymbol{u}}_j(\boldsymbol{x}, x^*)|^2\rangle_{\boldsymbol{x},i\neq j}}{2\langle|\widetilde{\boldsymbol{u}}_i(\boldsymbol{x}, x^*)|^2\rangle_{\boldsymbol{x},i}}, \tag{8}$$

where $\widetilde{\boldsymbol{u}}$ is the fluctuation velocity field, $\widetilde{\boldsymbol{u}} = \boldsymbol{u} - \langle\boldsymbol{u}\rangle_i$ and averages are done over all distinct pairs $i \neq j$ in the ensemble and over the entire domain $\boldsymbol{x}$. For completely uncorrelated velocity fields $\Delta\widetilde{u}^2(x^*) = 1$ [20]. The normalized correlation is $C = 1 - \Delta\widetilde{u}^2(x^*)$; it is zero for uncorrelated velocity fields. A similar error can be defined for the enstrophy. Notice that the domain average $\langle\cdots\rangle_{\boldsymbol{x}}$ in Eq. (8) must be done over the numerator and denominator separately. Without it, the resulting random field (with mean 1) signifies the independence of the experiment realizations.

The error energy and enstrophy are analogous to a structure function between different experiments. In addition, we define a structure function that quantifies the correlation of the vorticity fields *within* a single experimental field:

$$S(\delta, x^*) = \frac{\langle[\widetilde{\omega}_i(\boldsymbol{x}+\boldsymbol{\delta}, x^*) - \widetilde{\omega}_i(\boldsymbol{x}, x^*)]^2\rangle_{\boldsymbol{x},i}}{\langle\widetilde{\omega}_i^2(\boldsymbol{x}+\boldsymbol{\delta}, x^*)\rangle_{\boldsymbol{x},i} + \langle\widetilde{\omega}_i^2(\boldsymbol{x}, x^*)\rangle_{\boldsymbol{x},i}}, \tag{9}$$

and similarly for the velocity field. In Eq. (9) we take the separation $\boldsymbol{\delta} = \delta\,\boldsymbol{e}_x$, and we realize that the field $\omega(\boldsymbol{x}, x^*)$ is inhomogeneous; its statistical properties depend on $\boldsymbol{x}$. For a spatially incoherent field (such that $\langle\widetilde{\omega}(\boldsymbol{x}+\boldsymbol{\delta}, x^*)\,\widetilde{\omega}(\boldsymbol{x}, x^*)\rangle = 0$), $S = 1$, while for a homogeneous field $\widetilde{\omega}(\boldsymbol{x}, x^*)$ S is the (normalized) second order vorticity structure function. Similarly, the correlation function is $C = 1 - S$. Summarizing, we have the error enstrophy (and energy) to quantify the coherence *between* experiments, and the equivalent structure function S to express the coherence *within* a single realization.

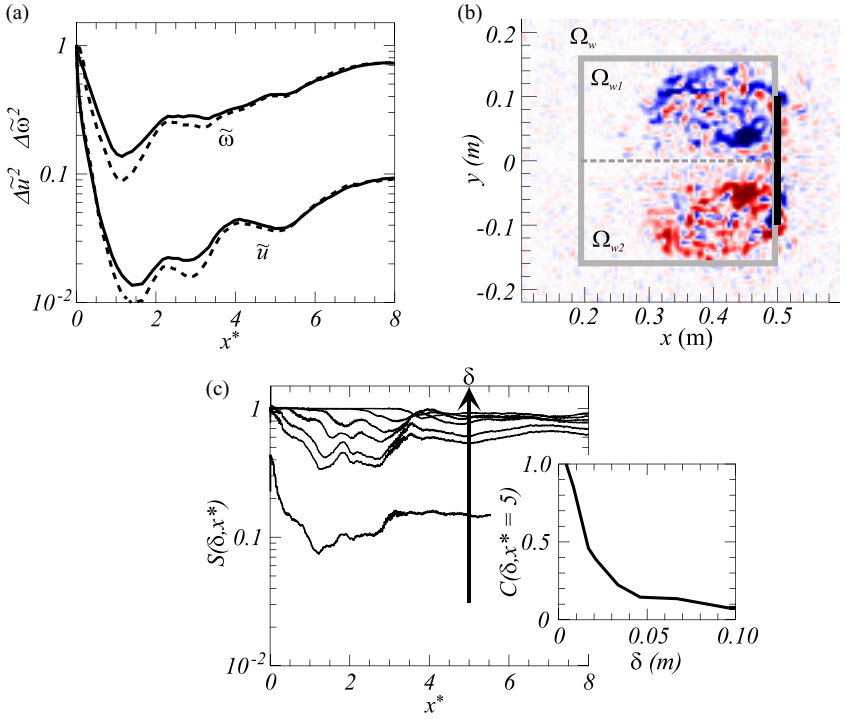

FIG. 5. Global characterization of the coherence between experiment realizations and the coherence inside experiments. (a) Ensemble- and space-averaged normalized error energy $\Delta\widetilde{u}^2(x^*)$ and enstrophy $\Delta\widetilde{\omega}^2(x^*)$. In the case of uncorrelated fields, $\Delta\widetilde{u}^2(x^*) = \Delta\widetilde{\omega}^2(x^*) = 1$. Full lines are for the entire field of view, dashed lines are for the wake, as defined in (b). (b) Delineating the turbulent wake. Shown is $\omega(\boldsymbol{x}, x^*)$ at $x^* = 5$ ($x = 0.5$). The wake region Ω_w is a box with sides $l_x = 0.3$ m and $l_y = 0.32$ m, with its right boundary separated from the plate by $l_{\mathrm{bl}} = 5 \times 10^{-3}$ m. (c) Second-order structure function $S(\delta, x^*)$ [Eq. (9)] for separations $\delta = 0.01, \ldots, 0.1$. Inset: correlation function $C = 1 - S(\delta, x^*)$ at $x^* = 5$.

The dependence of the error energy and enstrophy on traveled plate distance x^* is shown in Fig. 5(a). As time progresses, velocity and vorticity fields of different experiments become increasingly decorrelated. The error energy demonstrates that the velocity field remains correlated the longest, whereas the vorticity field becomes almost completely decorrelated at the end of a run, $x^* = 8$. Clearly, the small scales are much less correlated between experiments than the large-scale motion.

The error energy and enstrophy [Eq. (8)] in Fig. 5 are for the entire domain that contains the boundary layers on the plate, the (detached) vortices, the wake envelope, and its inside turbulence. We have singled out the wake region Ω_w as illustrated in Fig. 5(b). It excludes the boundary layer on the plate, whose width is approximately $\mathrm{Re}^{-1/2}\, l_b \approx 4 \times 10^{-4}$ m, which is (much) smaller than the vector spacing (4.2×10^{-3} m). As Fig. 5(a) illustrates, the correlation between experiment realizations remains if we exclude the vorticity (velocity) field attached to the plate.

Inside the wake, the vorticity field becomes increasingly decorrelated between experiments. *Within* an experiment realization, the turbulent wake is characterized by a finite correlation length, as plots of $S(\delta, x^*)$ and $C(\delta, x^*) = 1 - S(\delta, x^*)$ in Fig. 5(c) show. With correlation length $l \approx 0.025$ m, $u = 0.14\ \mathrm{m\,s^{-1}}$, and $C_\epsilon = 0.47$ [21], we estimate a turbulent dissipation rate $\epsilon = C_\epsilon u^3/l \approx 6 \times 10^{-5}\ \mathrm{m^2\,s^{-3}}$, and a Taylor scale Reynolds number $\mathrm{Re}_\lambda \approx 10^2$, which should be compared to $\mathrm{Re}^{1/2}$, with $\mathrm{Re} = 4 \times 10^4$. However, this comparison may have been stretched too far, as the turbulence inside the wake is far from homogeneous.

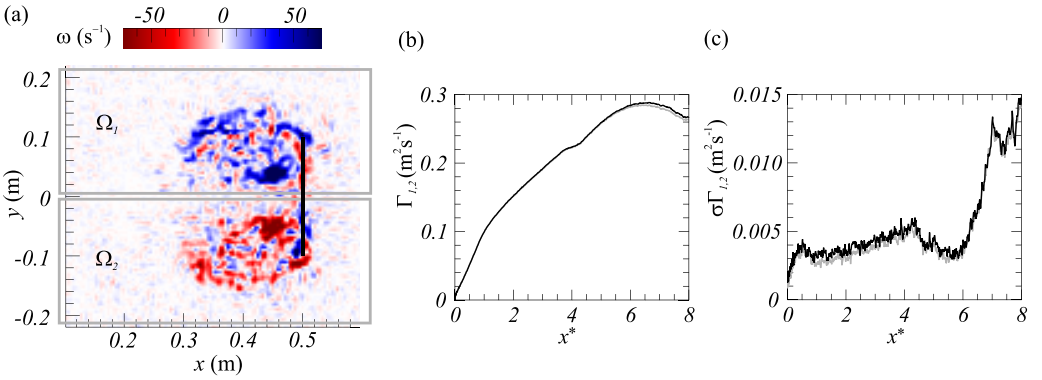

FIG. 6. (a) Instantaneous vorticity field for plate position $x^* = 5$. The circulations (per unit area) Γ_1 and Γ_2 are computed by averaging $\omega(\boldsymbol{x}, t)$ over the gray boxes Ω_1 and Ω_2, respectively. (b) Full line indicates ensemble mean $\langle\Gamma_1\rangle$, gray line $-\langle\Gamma_2\rangle$. The two mean circulations are almost perfectly symmetric. (c) R.m.s. circulation fluctuations; gray line: $\sigma\ \Gamma_1$, black line: $\sigma\ \Gamma_2$.

C. Circulation

While the pointwise fields $\Lambda_T(\boldsymbol{x}, x^*)$ and $d_T(\boldsymbol{x}, x^*)$ still display the vortical wake structure, we will now focus on the statistical properties of the circulation. Figure 6(a) illustrates the definition of the domains $\Omega_{1,2}$ used to compute the circulations $\Gamma_{1,2}(x^*)$. Throughout, the circulations are the domain-integrated vorticities,

$$\Gamma^i_{1,2}(x^*) = \int_{\Omega_{1,2}} \omega_i(\boldsymbol{x}, x^*)\, d^2\boldsymbol{x}.$$

Naturally, the ensemble averages are such that $\langle\Gamma_1\rangle > 0$ and $\langle\Gamma_2\rangle < 0$. The ensemble-mean circulations and their r.m.s. fluctuations,

$$\sigma\Gamma_{1,2} = \left\langle \left(\Gamma^i_{1,2} - \langle\Gamma^j_{1,2}\rangle_j\right)^2 \right\rangle_i^{1/2},$$

are shown in in Figs. 6(b) and 6(c). Remarkably, not only is the $y \leftrightarrow -y$ symmetry of the setup preserved in the mean, but also in the r.m.s. fluctuations. The symmetry is increasingly lost in higher order moments of the fluctuating circulation (such as the flatness), which is already evident from the vorticity fields in the domains Ω_1 and Ω_2 in Fig. 6(a).

The $y \leftrightarrow -y$ symmetry of the projections of the flow on the cross-sectional plane points to their common cause: the circulation of the entire large-scale trailing vortex loop [see Fig. 2(a)]. The two vortices are the intersections of this vortex loop with the measurement plane. A further analysis is provided in Fig. 7, where we plot Γ^i_2 as a function of Γ^i_1 for plate separations $x^* = 5$ and $x^* = 7$, and $i = 1, \ldots, 42$. The two circulations are almost perfectly anticorrelated. Incidentally, their fluctuations are approximately Gaussian. The flatness, $\langle(\Gamma^i_1 - \langle\Gamma^j_1\rangle_j)^4\rangle_i / \langle(\Gamma^i_1 - \langle\Gamma^j_1\rangle_j)^2\rangle_i$, which is 3 for a perfect Gaussian distribution, is 3 on average with r.m.s. variation 0.9.

The correlation between Γ_1 and Γ_2 as a function of the plate displacement x^* is shown in Fig. 7(c); it is approximately -1, which agrees with the $y \leftrightarrow -y$ symmetry of the circulation fluctuations. This (anti)symmetry is increasingly broken when the circulations are restricted to the wakes, $\Omega_{w\,1,2}$ [indicated in Fig. 5(b)] with increasing distance l_{bl}. It is clearly related to the vorticity layers that are attached to the plate. The correlation between the corresponding circulations $\Gamma_{w\,1}$ and $-\Gamma_{w\,2}$ revives at $x^* = 4$, when the vortex loop detaches from the plate, and again at $x^* > 6$, when the wake becomes fully turbulent.

At a traveled distance $x^* \approx 6$, as the wake becomes turbulent and the sign of the local vorticity starts to alternate, the measured flow also becomes three-dimensional. The two-dimensionality of

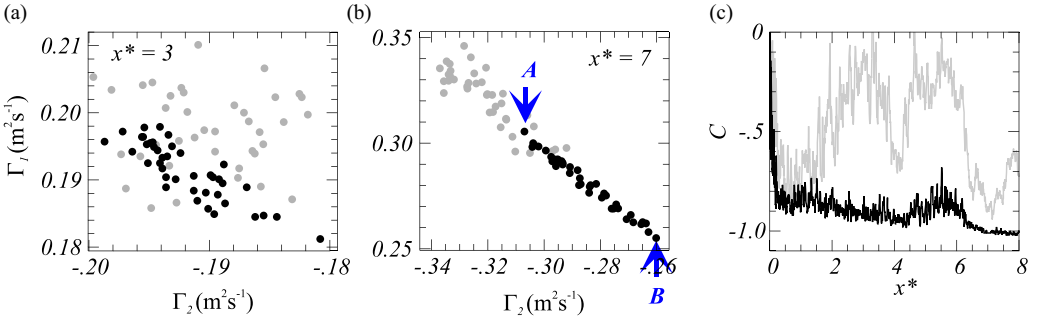

FIG. 7. (a, b) Γ_2 vs Γ_1 for all 42 experiment realizations at plate displacements $x^* = 3$ and $x^* = 7$, respectively. Black dots are circulations over the domains $\Omega_{1,2}$. The gray dots correspond to the circulation in the wake regions $\Omega_{w\,1}$ and $\Omega_{w\,2}$ [see Fig. 5(b)]. (c) Black line: correlation between Γ_1 and Γ_2, with circulations computed over the full domains Ω_1, Ω_2; gray line: with circulations in the wake regions $\Omega_{w\,1}$ and $\Omega_{w\,2}$.

the flow is quantified by the normalized divergence, $\zeta = \langle \nabla \cdot \boldsymbol{u}/(\nabla \boldsymbol{u} : \nabla \boldsymbol{u})^{1/2} \rangle$. A perfectly planar flow has $\zeta = 0$. We find that $|\zeta| \lesssim 0.02$ for $x^* \lesssim 6$, and rises to $\zeta \approx 0.06$ at $x^* = 8$ as the flow starts to explore the z dimension.

D. Extreme values

In Fig. 7(b) we have indicated the experiment realizations $i_{\min}$ (A) and $i_{\max}$ (B) where the circulations Γ_1 (and thus Γ_2) take on extreme values at $x^* = 7$. The question is whether these extreme events can be predicted from extreme events in the past ($x^* < 7$) of the circulation.

To this aim we replace the value of the 42 circulations $\Gamma_{1,2}$ at each plate displacement x^* with their rank $\Gamma'_{1,2}$: it is 1 for the largest circulation, 0 for the median, and -1 for the smallest one. When computing the correlation between circulations [including that of Fig. 7(c)], the transformation to ranks removes bias due to the magnitude of the circulation. Also, the correlation value is insensitive to a (nonlinear) transformation of the circulation. Incidentally, the difference with correlations using the physical values was negligible. Extreme events are now easy to trace: they are $\Gamma' = \pm 1$, irrespective of the physical value of Γ.

The first question is whether the circulation in an experiment, say i_0, that displays an extreme circulation at, say, x_0^*, remains extreme at other plate distances x^*. The answer to this question is provided by a plot of $\Gamma'^{\,i_0}_{1,2}(x^*)$. In Fig. 8(a) we show the trace of the circulations $\Gamma'_{1,2}$ of the experiment indicated by "A" in Fig. 7(b). At $x_0^* = 7$ the circulations take on extreme values: $\Gamma'_2 = -1$, $\Gamma'_1 = 1$ (indicated by the blue dots). Notice that the traces of Γ'_1 and Γ'_2 are almost symmetrical, in agreement with Fig. 7(b). In a small range around x_0^* the circulations remain extreme, but otherwise Γ'_2 stays smaller than the median, and Γ'_1 remains larger than the median. The experiment marked by "B" in Fig. 7(b) displays similar behavior. We conclude that an extreme circulation Γ'_1 is preceded by circulations larger than the median and vice versa for Γ'_2.

In case of completely random circulation fluctuations, Γ' would have equal probabilities to be 1 and -1. This is clearly not the case and suggests the presence of long-ranged correlations in a single experiment realization.

The normalized correlation $C_{x_0^*}(x^*)$ between $\Gamma'_1(x^*)$ and $\Gamma'_1(x_0^*)$ for $x_0^* = 5$ and $x_0^* = 7$ is shown in Fig. 8(c). It is defined similarly to Eq. (6) and is trivially 1 at $x^* = x_0^*$. At $x_0^* = 7$, inside the turbulent domain, it is sharply peaked, but drops to $C_{x_0^*}(x^*) \approx 0.5$ for earlier plate positions. The correlation of Γ'_2 is similar. The width (full width half maximum) of the peak is $\approx$0.1, which can be compared to the plate height l_b.

Since the time- (x^*-) dependent flow is nonstationary, it is not possible to define a correlation time (length), and correlations such as in Fig. 8(c) are the best we can do. From these correlation

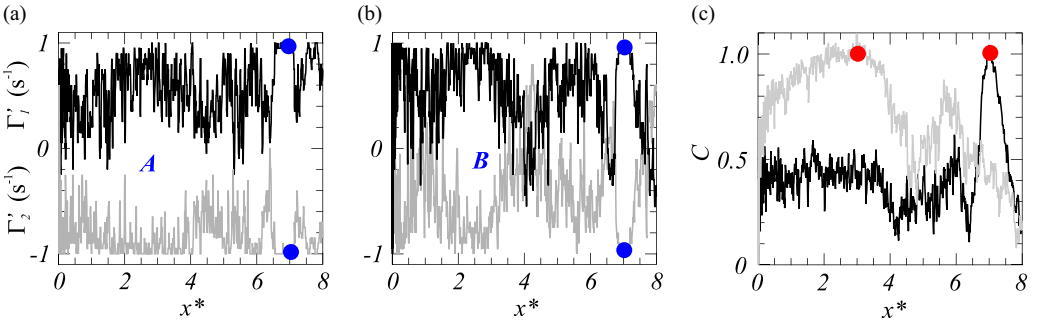

FIG. 8. (a, b) Traces of $\Gamma'_{1,2}(x^*)$ of selected experiments. Shown are the circulations after the rank transformation; the largest circulation in the ensemble takes on the value 1, the smallest is -1. (a) Black line: $\Gamma'_1(x^*)$ of the experiment indicated by "A" in Fig. 7(b), where Γ_1 and $|\Gamma_2|$ are minimal. Gray line: same but for $\Gamma'_2(x^*)$. The two traces are approximately each other's mirror. (b) Same as (a), but for point "B" in Fig. 7(b), where Γ_1 and $|\Gamma_2|$ are maximal. (c) Black curve: correlation between $\Gamma'_1(x_0^*))$ with $\Gamma'_1(x^*)$ for $x_0^* = 7$. Gray line: the same but for $x_0^* = 3$. The correlations are trivially 1 for $x^* = x_0^*$ (indicated by the red dots).

functions it can be concluded that vorticity fields at $x_0^* \lesssim 6$ are correlated with those at $x^* \lesssim x_0^*$, but once the flow enters the turbulent state ($x_0^* > 6$) correlations are restricted to a narrow interval in x^*.

IV. CONCLUSION

In the plane of observation, the wake behind a traveling plate evolves from ordered vortex pairs to turbulence. We study the statistics of this transition by repeating the experiment many times. The variability of the ensemble of experiments can be predicted from observation of the finite-time Lyapunov exponents of a single experiment. More specifically, the ensemble-averaged FTLE field can be reconstructed from observing the variation between experiments and vice versa.

As time progresses, the correlation between the vorticity fields of different experiments decreases, both for the entire field and for the turbulent wake. The mean and fluctuating circulations computed over the upper and lower halves of the observed domain are almost perfectly (anti)symmetric. It reflects the (anti)correlation of the instantaneous values of Γ_1 and Γ_2. However, this no longer holds for the circulations restricted to the turbulent wake.

There has been beautiful numerical work on the first stages of the wake vortex formation [2,4,7]. We hope that this work inspires the numerical exploration of the turbulent regime.

ACKNOWLEDGMENTS

The expertise on PIV of E. Overmars was essential for this project. The assistance of J. Graafland and J. Ruijgrok is greatly appreciated. G. Mulder helped manage the robot. This work is part of the "Impulsive Flows" project, which has received funding of the European Research Council (ERC) under the EU Horizon 2020 program (Grant No. 884778).

[1] L. Prandtl, Über Flüssigkeitsbewegung bei sehr kleiner Reibung, in *Verhandlungen des III. Internationalen Mathematiker-Kongresses*, Vol. 904 (Leipzig: B. G. Teubner 1904, pp. 484–491.

[2] P. Koumoutsakos and D. Shiels, Simulations of the viscous flow normal to an impulsively started and uniformly accelerated flat plate, J. Fluid Mech. **328**, 177 (1996).

[3] J. N. Fernando and D. E. Rival, On vortex evolution in the wake of axisymmetric and non-axisymmetric low-aspect-ratio accelerating plates, Phys. Fluids **28**, 017102 (2016).
[4] P. Luchini and R. Tognaccini, The start-up vortex issuing from a semi-infinite flat plate, J. Fluid Mech. **455**, 175 (2002).
[5] M. Gharib, E. Rambod, and K. Shariff, A universal time scale for vortex ring formation, J. Fluid Mech. **360**, 121 (1998).
[6] L. Xu and M. Nitsche, Start-up vortex flow past an accelerated flat plate, Phys. Fluids **27**, 033602 (2015).
[7] L. Xu and M. Nitsche, Scaling behaviour in impulsively started viscous flow past a finite flat plate, J. Fluid Mech. **756**, 689 (2014).
[8] See Supplemental Material at http://link.aps.org/supplemental/10.1103/PhysRevFluids.8.104601 for the vorticity field behind a traveling plate as it evolves into turbulence. The experiment is repeated 42 times; realization 1 is left and 42 is right.
[9] G. Haller and G. Yuan, Lagrangian coherent structures and mixing in two-dimensional turbulence, Physica D **147**, 352 (2000).
[10] S. C. Shadden, F. Lekien, and J. E. Marsden, Definition and properties of Lagrangian coherent structures from finite-time Lyapunov exponents in two-dimensional aperiodic flows, Physica D **212**, 271 (2005).
[11] T. Bohr, M. H. Jensen, G. Paladin, and A. Vulpiani, *Dynamical Systems Approach to Turbulence*, Cambridge Nonlinear Science Series, Vol. 7 (Cambridge University Press, Cambridge, 1998), p. 301.
[12] J. Bedrossian, A. Blumenthal, and S. Punshon-Smith, The Batchelor spectrum of passive scalar turbulence in stochastic fluid mechanics at fixed Reynolds number, Commun. Pure Appl. Math. **75**, 1237 (2021).
[13] Y. Xiang, Z. Li, S. Qin, and H. Liu, Formation number and pinch-off signals of disc vortex ring based on a Lagrangian analysis, Exp. Therm Fluid Sci. **129**, 110452 (2021).
[14] M. J. Twardos, P. E. Arratia, M. K. Rivera, G. A. Voth, J. P. Gollub, and R. E. Ecke, Stretching fields and mixing near the transition to nonperiodic two-dimensional flow, Phys. Rev. E **77**, 056315 (2008).
[15] J. Reijtenbagh, J. Westerweel, and W. van de Water, Large-scale structures of scalar and velocity in a turbulent jet flow, Phys. Rev. Fluids **6**, 084611 (2021).
[16] J. Eisma, J. Westerweel, and W. van de Water, Do coherent structures organize scalar mixing in a turbulent boundary layer? J. Fluid Mech. **929**, A14 (2021).
[17] E. J. Grift, N. B. Vijayaragavan, M. J. Tummers, and J. Westerweel, Drag force on an accelerated submerged plate, J. Fluid Mech. **866**, 369 (2019).
[18] U. Frisch, *Turbulence: The Legacy of A. N. Kolmogorov* (Cambridge University Press, Cambridge, 1995).
[19] B. Galanti and A. Tsinober, Is turbulence ergodic? Phys. Lett. A **330**, 173 (2004).
[20] G. Boffetta and S. Musacchio, Chaos and predictability of homogeneous-isotropic turbulence, Phys. Rev. Lett. **119**, 054102 (2017).
[21] B. R. Pearson, P. Å Krogstad, and W. van de Water, Measurements of the turbulent energy dissipation rate, Phys. Fluids **14**, 1288 (2002).